Article

Discharge Experiment and Structure Optimisation Simulation of Impulse Sound Source

Xu Gao [1,2]**, Jing Zhou** [1,2,]*****, Haiming Xie** [2] **and Xiao Du** [1,2]

1   College of Petroleum Engineering, Xi'an Shiyou University, Xi'an 710065, China;
    20111010002@stumail.xsyu.edu.cn (X.G.); 22111010007@stumail.xsyu.edu.cn (X.D.)
2   National Engineering Laboratory for Oil and Gas Drilling Technology, Xi'an Shiyou University,
    Xi'an 710065, China; haimingxie@xsyu.edu.cn
*   Correspondence: jzhou@xsyu.edu.cn

Abstract: The wave frequency and energy of traditional piezoelectric emission sources used in acoustic logging are limited, which results in an inadequate detection resolution for measuring small-scale geological formations. Additionally, the propagation of these waves in formations is prone to loss and noise interference, restricting detection to only a few tens of meters around the well. This paper investigates an impulse sound source, a new emission source that can effectively enhance the frequency range and wave energy of traditional sources by generating excitation waves through high-voltage discharges in a fluid-penetrated electrode structure. Firstly, a high-voltage circuit experimental system for the impulse sound source was constructed, and the discharge and response characteristics were experimentally analyzed. Then, four types of needle series electrode structure models were developed to investigate and compare the effects of different electrode structures on the impulse sound source, with the needle-ring electrode demonstrating superior performance. Finally, the needle-ring electrode structure was optimized to develop a ball-tipped needle-ring electrode, which is more suitable for acoustic logging. The results show that the electrode structure directly influences the discharge characteristics of the impulse sound source. After comparison and optimization, the final ball-tipped needle-ring electrode exhibited a broader frequency range—from zero to several hundred thousand Hz—while maintaining a high acoustic amplitude. It has the capability to detect geological areas beyond 100 m and is effective for evaluating micro-fractures and small fracture blocks near wells that require high detection accuracy. This is of significant importance in oil, gas, new energy, and other drilling fields.

Keywords: impulse sound source; electrode structure; amplitude; frequency; needle-ring electrode

1. Introduction

Acoustic logging is a widely used logging technique. The acoustic field data recorded by acoustic logging can be used to obtain formation parameters [1], to evaluate cementing quality [2], and to obtain the acoustic field response of structures adjacent to the wellbore. This allows the properties and extent of formation interfaces, fractures, and other reservoir spaces to be determined, facilitating the exploration of oil, gas, and mineral resources [3,4]. In recent years, the focus of oil and gas field exploration and its development has gradually shifted to finding unconventional, small, and potential oil and gas resources. The development of acoustic logging tools with high accuracy and long detection ranges has become a key issue.

The detection accuracy and depth of acoustic logging are related to the amplitude and frequency of the transmitting sound source. The greater the amplitude and the lower the frequency of the transmitting sound source, the greater the detection depth—conversely, the greater the amplitude and the higher the frequency, the greater the detection accuracy. Currently, the mainstream emitted sound source is a piezoelectric transducer. Many

scholars have invested in the research of bandwidth optimization and amplitude optimization of piezoelectric transducers. Recent advances in piezoelectric materials (e.g., lead zirconate titanate (PZT) and composites) [5,6] and piezoelectric actuator design [7] have led to the improved frequency stability and bandwidth of transducers, resulting in improved logging performance.

In the field of acoustic logging, commonly used transmitting sound sources include unipolar transducers, dipole transducers, phased-array transducers, and multipole transducers, with a frequency distribution of 0–25 kHz and a detection area of several tens of meters [8,9].

Monopole transducers are not source-directed, have a frequency range of 10 kHz–20 kHz, and the detection range is typically within a dozen meters [10,11]. The dipole transducer has a frequency range of 0.5 kHz–5 kHz, a detection range of up to tens of meters, and a directional acoustic field that is axisymmetric with a 180° uncertainty in the azimuthal description [12,13]. Multipole transducers are capable of acquiring unipolar, dipole, and quadrupole sound field data. The frequency range is 15 kHz–25 kHz [14,15] and generally captures ground wave information over a regional area of tens of meters around the borehole. The directivity of the quadrupole sound field excited by a quadrupole source is generally left–right symmetric [16]. The wave amplitude of the quadrupole source is low, and the useful information data of the formation are sometimes disturbed and covered by noise, which affects normal measurements and drilling [17,18]. Circumferential measurements with phased-array transducers are achieved by arranging multiple point sound sources in a specific pattern and applying different excitation information to each point sound source as needed, thereby achieving directional excitation and detection [19]. The China University of Petroleum, in collaboration with the logging company CNPC, has developed directional detection instruments based on phased-array transducers. These instruments have detection ranges of up to 10 m in liquid media and 40 m in solid formations [20,21]. When performing circumferential measurements with phased-array transducers, the initial excitation and energy transmission outside the well are limited. The frequency is mainly around 14 kHz, and the detection range is about tens of meters [22].

With the technological update and iteration of the transmitting sound source, the accuracy and application range of acoustic wave transmission measurements in subsurface structures have been gradually improved, and the detection range has been extended from a few meters to tens of meters. However, due to the limitations of the frequency band and wave amplitude, it is still unable to guide the identification of tiny cracks in near-well zones, the connectivity of long-distance relief wells, the detection of stratigraphic boundaries in far-well zones, and so on. Impulse sources have significant advantages over other sources for geological surveys of areas close to the borehole and in front of the drill bit. The higher amplitude and wider frequency band provide high accuracy and a wide detection range for subsurface exploration. Impulse sound sources use high-voltage circuits to provide energy and transmit it to electrodes, causing shock wave discharge in the liquid and generating a strong acoustic pulse response. This shock wave has greater amplitude and more abundant energy. When combined with a reflective focusing cover, it can achieve sound source directionality [23], and its frequency range is broad, reaching from 0 Hz to 100 kHz.
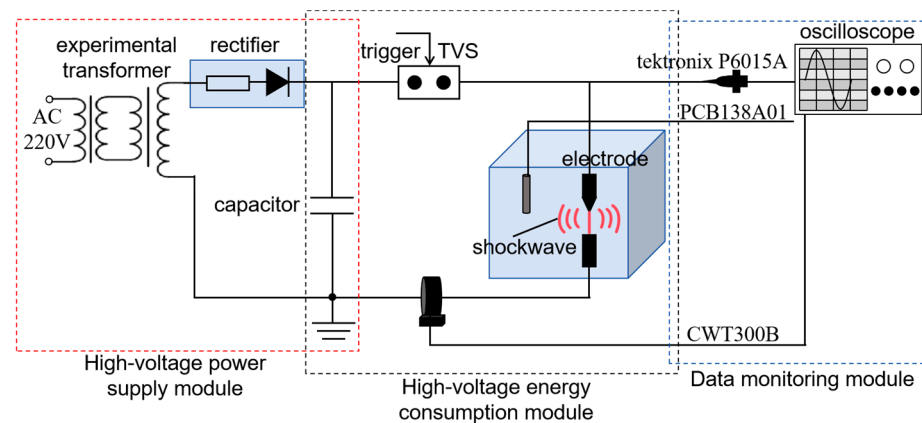
The electrode structure is the carrier and core of the impulse sound source responding to the discharge process. It is also the transducer that converts electrical energy into acoustic energy, which directly affects the wave amplitude and frequency band characteristics of the acoustic wave and then affects the range and accuracy of the impulse sound source for detecting geological formations next to the well. Firstly, we designed and set up a high-voltage circuit experimental system for the impulse sound source. Then, we investigated the electrode characteristics of the impulse sound source through experiments and numerical simulations. We then compared it to various electrode structures to find an electrode structure that can produce more energy, has a wide frequency band, small size, and can be mounted on the drill collar, which can further provide a reference basis for the research of the impulse sound source and provide realistic bases for the design of the sound source of

the acoustic wave sounding instrument that is used for deeper and more accurate sounding along with the drilling.

2. Experiment

2.1. Principle

A high-voltage experimental platform for impulse sound sources was constructed, which can provide a working environment for impulse sound sources and measure their performance in real time. Figure 1 shows the working circuit diagram of the high-voltage experimental platform for the impulse sound source. It mainly consists of a high-voltage power supply module, a high-voltage energy consumption module, and a data monitoring module.

Figure 1. Working circuit diagram of the high-voltage experimental platform for impulse sound source.

Figure 2 shows the high-voltage power supply module, which includes a voltage regulator, booster, current limiting resistor, silicon stack, and high-voltage capacitor. The 220 V AC voltage is connected and then boosted to several kilovolts by the voltage regulator and booster, then rectified to DC to feed the capacitor directly. When the voltage across the capacitor reaches 20 kV, the voltage regulator is switched off, completing the energy storage process.
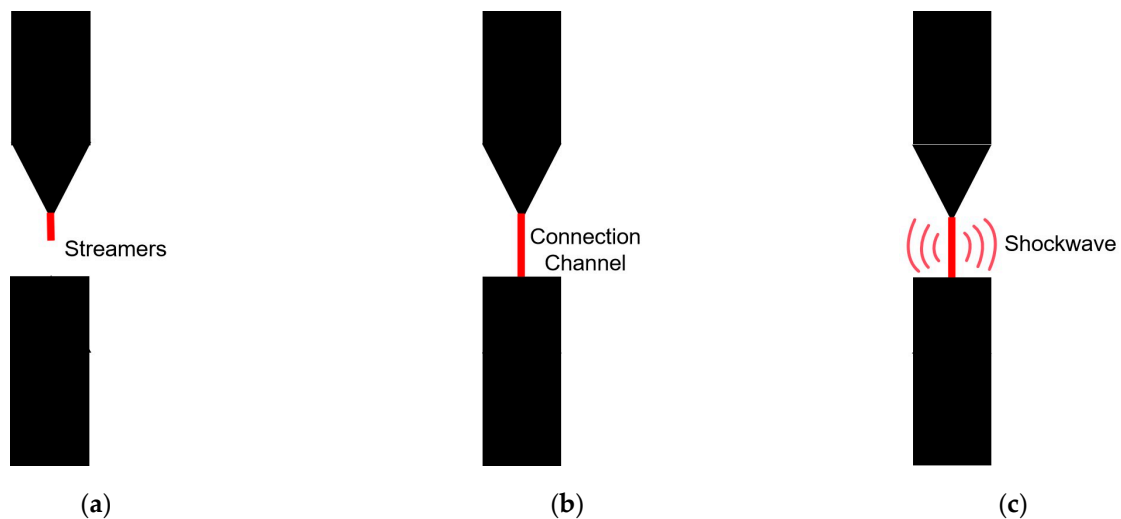

Figure 2. Physical diagram of high-voltage power supply module.

The high-voltage energy consumption module includes a high-voltage capacitor, a high-voltage discharge switch, and a discharge load. When the trigger control switch is closed, the capacitor releases a large amount of energy, which is then transferred to and applied to the discharge load immersed in tap water. The discharge load was set up with a needle-bar electrode structure, as shown in Figure 3, and its geometrical parameters are shown in Table 1. The needle-bar electrode is cast in an insulated material and contained in a stainless-steel cylinder, which is made of two parts and connected by three stainless-steel

supports. As shown in Figure 4, during the high-voltage pulse shock wave discharge of the needle-bar electrode in water, the discharge process can be roughly divided into three stages: pre-breakdown stage, during-breakdown stage, and post-breakdown stage. The pre-breakdown stage is the initial phase of the needle-bar electrode shock wave discharge. In this phase, the needle-bar electrode gradually generates streamers under the influence of high-voltage energy. These streamers expand and grow with a continuous energy supply, entering the breakdown stage. Then, the streamers from the needle electrode and the bar electrode meet to form a conductive channel, leading to a breakdown. In the post-breakdown stage, the high-temperature, high-pressure conductive channel expands, generating shock waves due to the incompressibility of the surrounding liquid water medium.

Figure 3. Needle-bar electrode structure.

Figure 4. Needle-bar electrode wave generation process: (**a**) The pre-breakdown stage; (**b**) the during-breakdown stage; (**c**) the post-breakdown stage.

The data monitoring module performs the real-time monitoring and acquisition of the entire shock wave discharge process. The shock wave discharge voltage is captured by the high-voltage probe P6015A (Tektronix, Beaverton, OR, USA). The shock wave discharge current is detected by the current probe CWT300B (Power Electronic Measurements Ltd., Long Eaton, UK). The pressure probe 138A01 (PCB Piezotronics, Buffalo, NY, USA) is fixed in the tap water tank, oriented horizontally and parallel to the discharge center of the needle-bar electrode, allowing it to measure the transient pulse shock pressure wave
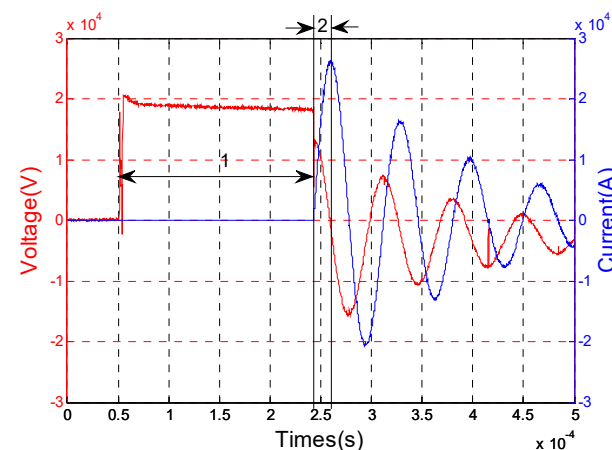
generated by the high-voltage discharge process. The voltage and current at both ends of the electrode, as well as the pulse shock pressure wave, are recorded by the oscilloscope to capture the waveforms and store the data.

Table 1. Geometrical parameters of needle-bar electrode.

Part	Geometrical Parameters
Bottom radius of the cone	0.5 mm
Top radius of the cone	5 mm
Height of the cone	20 mm
Height of the needle column	50 mm
Radius of bar electrode	5 mm
Height of bar electrode	0.5 mm

2.2. Results

The voltage and current waveforms measured across the electrodes during discharge, as captured by the oscilloscope, are shown in Figure 5. The pre-breakdown stage of the shockwave discharge process for the needle-bar electrode is indicated as 1 in Figure 5, with a duration of 0.19 ms and a breakdown voltage of 18.5 kV. During the breakdown and post-breakdown stages, accompanied by strong shockwave discharge, the voltage across the electrodes drops rapidly in the region marked as 2 in Figure 5, while the current rises sharply, peaking at 25.8 kA. Subsequently, the current across the electrodes decays through circuit oscillations until the amplitude reaches zero.

Figure 5. Voltage and current waveforms of needle-bar electrode.

During the post-breakdown stage, a connecting channel forms in the gap between the needle and bar electrodes, which diffuses and emits a strong shockwave. The actual shockwave pressure value is related to the voltage measured by the oscilloscope according to the conversion relationship shown in Equation (1).

$$P = U_e/a \ (Pa) \tag{1}$$

where U_e is the voltage value measured by the oscilloscope; a is the sensitivity of the pressure sensor; P is the actual pressure value of the shockwave. The pressure–time curve of the shockwave is shown in Figure 6.

From Figure 6, it can be seen that the peak pressure of the needle-bar electrode shock wave discharge is 14.02 MPa. Moreover, it can maintain a high intensity for an extended period of time.
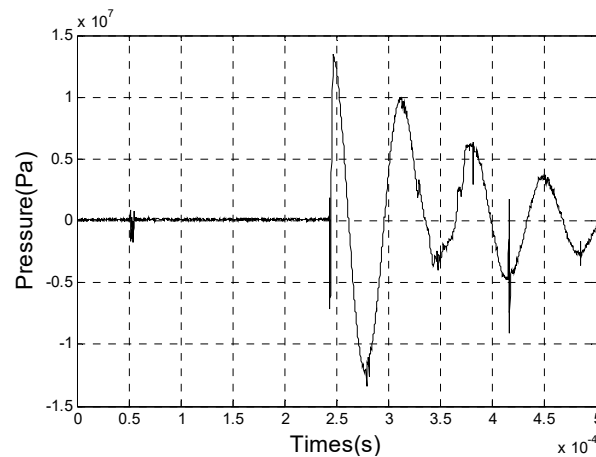
Figure 6. Pressure–times curve of the shockwave.

3. Comparison

The impulse sound source has a strong amplitude, is controllable, has a wide bandwidth, and has directivity performance. It is a good solution to the current use of traditional sound source logging. However, there are two problems: firstly, the detection outside the well is not deep; secondly, the accuracy is not high. The impulsive sound source electrode structure is different, and the drilling impulsive sound source generates impulsive wave characteristics that are different. Therefore, it is necessary to study the characteristics of the electrode structure in depth, from which we can find an electrode structure with a high amplitude, wide frequency band, and small volume that can be applied to the drill collar and used as a reference in the design of a sound source for drilling acoustic sound wave detection instruments. The needle electrode has a simple structure and a size suitable for the narrow spaces of downhole instruments, and it offers high electro-acoustic energy conversion efficiency. It is widely used by researchers to study discharge phenomena and mechanisms in underwater pulse discharges [24,25]. Based on the cylindrical channel theory, simulations were conducted on four types of needle electrodes to investigate the amplitude of the shockwave at the moment of plasma discharge breakdown in water.

3.1. Theory

When the electrode breaks down, a cylindrical connecting channel is formed between the electrodes. Assuming the channel is an ideal gas, the shockwave pressure can be described using the gas equation [26]:

$$P = nkT - \frac{\mu_0 i^2}{8\pi^2 R} - \frac{e^2}{32\pi^2 \varepsilon_0}\left(\frac{4\pi n}{3}\right)^{4/3} \tag{2}$$

where n, k, and ε_0 are constants; T is the column channel temperature; μ_0 generally takes the value of $4\pi \times 10^{-7}$ H/m; i is the column channel current; R is the column channel resistance; and e is the unit charge electricity.

The strength of the shockwave can be expressed by taking the logarithm of its effective value:

$$SPL = 20\lg\frac{P}{P_e} \tag{3}$$

The high-voltage supply releases the energy stored in the capacitor:

$$E = \frac{1}{2}CU_0^2 \tag{4}$$

where C is the capacitance, and U_0 is the supply voltage.

The shockwave generates intense energy, which can be expressed as follows [27]:

$$E_S = \frac{4\pi d^2}{\rho C_0} \int_0^T p(t)^2 dt = \frac{4\pi dM^2}{\rho C_0} \int_0^t U(t)^2 dt \tag{5}$$

where ρ is the density of water; C_0 is the speed of sound in water; $p(t)$ is the shock-wave pressure; M is the sensitivity of the hydrophone; and $U(t)$ is the voltage signal of the hydrophone.

The efficiency of the impulse sound source in converting from electrical energy to acoustic energy is
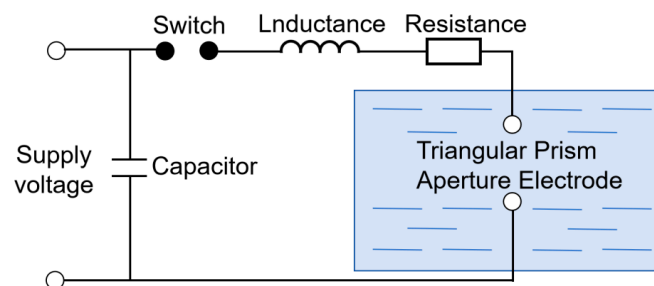
$$\eta = \frac{E_s}{E} \tag{6}$$

3.2. Conditions

For simulation purposes, the overall circuit of the electrode high-voltage circuit experiment was simplified to an equivalent circuit, as shown in Figure 7, where the electrode was placed in the center of a rectangular liquid-filled box with a side length of 35 cm. The box was filled with tap water, the initial temperature of the water was 293.15 K, and the relative dielectric constant of the water was 81. The rated capacitance of the energy storage capacitor was C = 15 µF, the two ends of the electrodes were connected to the output end of the circuit, and the voltage at the two ends of the capacitor was set to 20 kV. All of the set parameters were consistent with the parameters of the previous experimental section, as shown in Table 2. The values of the external circuit resistance and inductance in the equivalent circuit can be calculated based on the current waveforms of the experiments in the previous section [28]. The inductance value is calculated using Equation (7), and the external circuit resistance is calculated using Equation (8).

$$\Omega = \sqrt{1/LC} = \frac{2\pi}{T_1} \tag{7}$$

$$\frac{I_{PP1}}{I_{PP2}} = e^{\frac{RT_1}{4L}} \tag{8}$$

where I_{PP1}, I_{PP2}, and T_1 are the first peak value, the second peak value, and the period value of the current waveform at both ends of the measured needle-bar electrodes for one cycle; the value of L was calculated to be 8.18 µH; the value of R was calculated to be 0.22 Ω.

Figure 7. Equivalent circuit diagram of impulse sound source discharge.

Table 2. External circuit parameters.

External Circuit	Parameters
Charging voltage	20 kV
Energy storage capacitance	15 µF
Equivalent inductance	8.18 µH
Equivalent resistance	0.22 Ω
Electrical conductivity	0.07 S/m
Relative dielectric constant of water	81

3.3. Validation

A structural simulation model of the needle-bar electrode of the impulse sound source with geometrical parameters consistent with the experiment was constructed using finite element software, as shown in Figure 8. The needle-bar electrode is located in a square tank, and the external circuit is set up as an impulse sound source discharge circuit equivalent to that of the experiment. To simulate the needle-bar electrode, a charging voltage of 20 kV was applied to the external circuit to induce the breakdown of the needle-bar electrode, and the voltage and current waveforms of the electrode in the pre-breakdown stage, the current waveforms in the post-breakdown stage, and the amplitude-time diagrams of the impulse waveforms of this electrode were obtained, as shown in Figure 9.
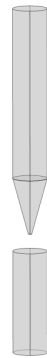

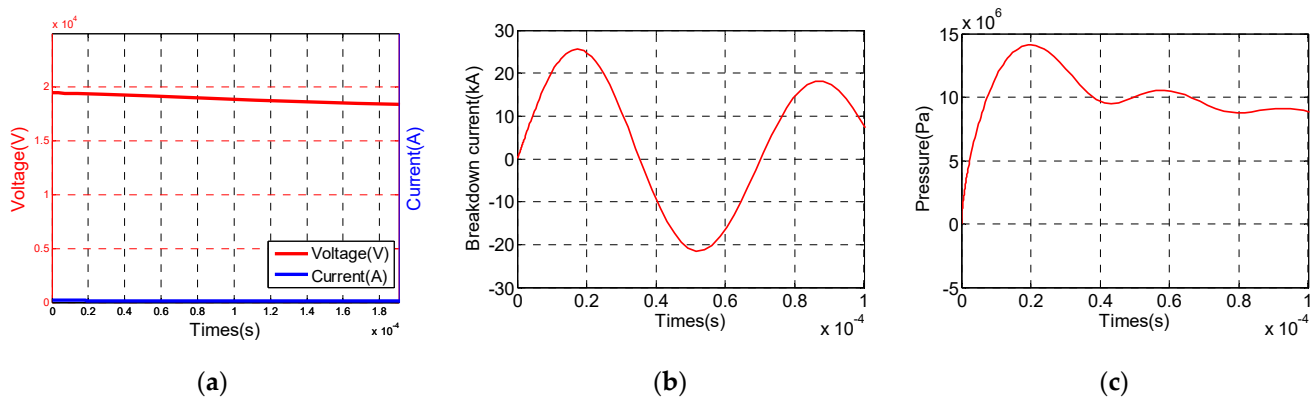**Figure 8.** Structural simulation model of the needle-bar electrode.

(a) **(b)** **(c)**

Figure 9. (**a**) Voltage and current waveforms of the needle-bar electrode at the pre-breakdown stage; (**b**) current waveform of needle-bar electrode in the post-breakdown stage; (**c**) pressure–time diagram of impulse wave.

Table 3 shows the parameters of the high-voltage experimental and simulation results for the needle-bar electrode. It can be observed that the simulation results are generally consistent with the experimental results, demonstrating the feasibility of the electrode simulation model and method.

Table 3. Parameters of the high-voltage experimental and simulation results.

Part	Experimental Results	Simulation Results
Pre-breakdown time	0.19 ms	0.19 ms
First peak of breakdown current	25.8 kA	25.58 kA
Amplitude of impulse wave	14.02 MPa	14.1 MPa
Breakdown voltage	18.50 kV	18.86 V

In Table 3, the experimental and simulation results are generally consistent, but there are still minor deviations. The simulation set all parameters to ideal states, but the

experiment cannot guarantee them completely. For example, (1) the tap water used in the experiment was laboratory firewater, which may have slight differences in liquid discharge characteristics compared to regular tap water, and (2) the repeated use of experimental devices may have caused wear and tear.

3.4. Modeling

Simulation models of the needle-ball electrode, needle-needle electrode, and needle-ring electrode structures were constructed. Apart from the different electrode structures, the rest of the parameters are kept the same. The circuit parameters are the same as the experiments in the previous section; the electrodes are all located in the water tank, and the external circuit is set up as an impulse sound source discharge circuit equivalent to the experiments.

3.4.1. Needle-Ball Electrode

The geometry of the constructed needle-ball electrode is shown in Figure 10, and the specific parameters of its dimensions are shown in Table 4.

Figure 10. Structural simulation model of the needle-ball electrode.

Table 4. Geometrical parameters of needle-ball electrode.

Part	Geometrical Parameters
Bottom radius of the cone	0.5 mm
Top radius of the cone	5 mm
Height of the cone	20 mm
Height of the needle column	50 mm
Radius of ball electrode	4 mm

3.4.2. Needle-Needle Electrode

The geometry of the constructed needle-needle electrode is shown in Figure 11, and the specific parameters of its dimensions are shown in Table 5.

Figure 11. Structural simulation model of the needle-needle electrode.

Table 5. Geometrical parameters of needle-needle electrode.

Part	Geometrical Parameters
Bottom radius of the cone	0.5 mm
Top radius of the cone	5 mm
Height of the cone	20 mm
Height of the needle column	50 mm

3.4.3. Needle-Ring Electrode

The geometry of the constructed needle-ring electrode is shown in Figure 12, and the specific parameters of its dimensions are shown in Table 6.

Figure 12. Structural simulation model of the needle-ring electrode.

Table 6. Geometrical parameters of needle-ring electrode.

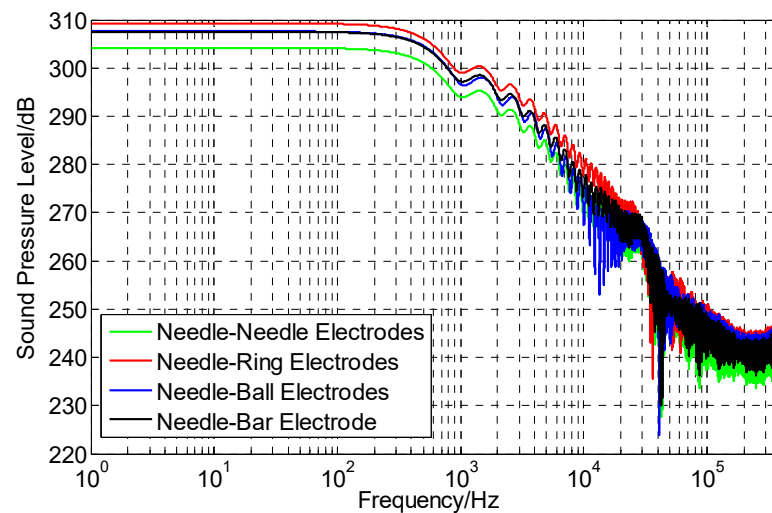| Part		Geometrical Parameters
Bottom radius of the cone		0.5 mm
Top radius of the cone		5 mm
Height of the cone		20 mm
Height of the needle column		50 mm
Ring electrode	Inner ring radius	5 mm
	Outer ring radius	6 mm

3.5. Option

As shown in Table 7, the pre-breakdown time, breakdown voltage, maximum discharge current, and impulse wave amplitude of several electrode structures were obtained after the experimental and simulation model calculations for the needle-bar electrode, needle-ball electrode, needle-needle electrode, and needle-ring electrode. The electro-acoustic efficiency was calculated by applying Equations (4)–(6). From Table 7, it can be seen that the electrode structure, as the discharge load of the impulse sound source, can directly affect the performance of the impulse sound source. The needle-ring electrode has a shorter pre-breakdown time, higher breakdown voltage, higher discharge current, stronger impulse wave amplitude, and higher electro-acoustic conversion efficiency.

The impulse wave amplitude of the needle-bar electrode, needle-ball electrode, needle-needle electrode, and needle-ring electrode can be converted into a sound pressure level using Equation (3). The FFT transform of the result can be used to obtain the sound pressure level–frequency diagrams of different electrode structures, as shown in Figure 13. From Figure 13, it can be seen that the frequencies of the impulsive waves generated by the four needle series electrode structures are similar. The needle-ring electrode is the highest, with an excellent performance in the range of 0 to 100 kHz, with a sound pressure level of more than 230 dB, indicating that the needle-ring electrode has the amplitude-frequency characteristics of a wide bandwidth and high amplitude.

Table 7. Comparison of needle series electrode structures.

Electrode Structures	Pre-Breakdown Time	Breakdown Voltage	Maximum Discharge Current	Maximum Impulse Wave Amplitude	Electro-acoustic Conversion Efficiency
Needle-Needle Electrode	537.03 μs	10.05 kV	10.6 kA	11.11 MPa	0.85%
Needle-Ring Electrode	229.09 μs	18.96 kV	26.5 kA	20.73 MPa	2.56%
Needle-Ball Electrode	269.15 μs	18.83 kV	20.5 kA	13.88 MPa	1.84%
Needle-Bar Electrode	190.00 μs	18.50 kV	25.8 kA	14.02 MPa	1.96%

Figure 13. Sound pressure level–frequency plots for needle series electrode structures.

In the needle series electrode structure, the amplitude of the impulse wave of the needle-ring electrode is higher, has a greater electro-acoustic conversion efficiency, and has the characteristics of a wide bandwidth and high amplitude, with a frequency band range of 0–100 kHz, which is more suitable for acoustic logging while drilling.

4. Discussion

4.1. Optimization

Considering the large radius of curvature of the ball electrode, which results in a significantly non-uniform electric field and denser space charge, we optimized the needle-ring electrode structure by incorporating the ball electrode. As shown in Figure 14, we constructed a model of the ball-tipped needle-ring electrode. Specifically, a sphere was added to the tip of the needle's electrode in the needle-ring electrode to form the ball-tipped needle-ring electrode. The specific geometric parameters are given in Table 8.
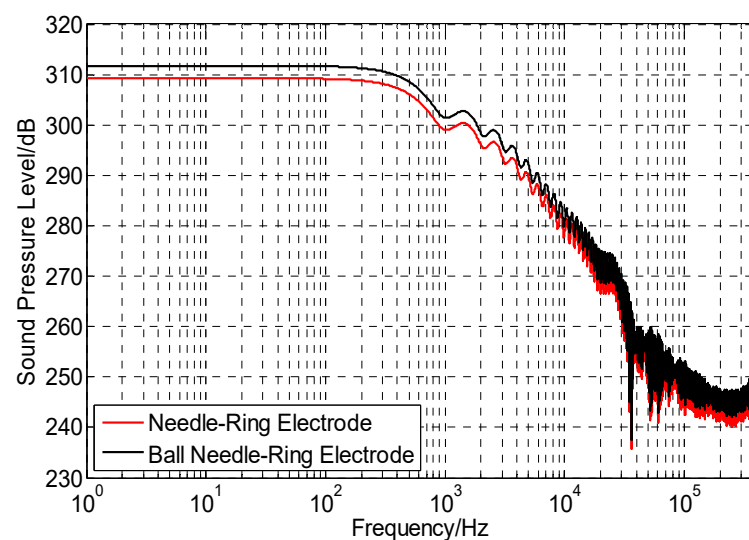

(**a**)   (**b**)

Figure 14. (**a**) Ball-tipped needle-ring electrode; (**b**) partial view of the cone head of the needle electrode.

Table 8. Geometrical parameters of ball-tipped needle-ring electrode.

Part		Geometrical Parameters
Bottom radius of the cone		0.5 mm
Top radius of the cone		5 mm
Height of the cone		20 mm
Height of the needle column		50 mm
Radius of the ball		0.5 mm
Ring electrode	Inner ring radius	5 mm
	Outer ring radius	6 mm

The same external circuit conditions as the experimental parameters were used to simulate the ball-tipped needle-ring electrode. As shown in Table 9, the performance parameters of the ball-tipped needle-ring electrode and the needle-ring electrode are compared. Due to the addition of a ball at the tip of the pair of needle electrodes, the inhomogeneous electric field generated at the tip increases, accelerating the heating rate and making it easier to form a connecting channel between the electrodes; thus, the pre-breakdown time of the ball-tipped needle-ring electrode is shorter than that of the needle-ring electrode. The shorter the pre-breakdown time, the higher the corresponding breakdown voltage, and the higher the impulse wave amplitude can be obtained. At the same time, the optimized electro-acoustic conversion efficiency is increased.

The amplitudes of the impulse wave at the ball-tipped needle-ring electrode and the needle-ring electrode were converted to the sound pressure level using Equation (3), followed by an FFT transform. The sound pressure level–frequency diagram is plotted as shown in Figure 15. When the frequency is constant, the impulse sound pressure level of the ball-tipped needle-ring electrode is greater than that of the needle-ring electrode. The sound pressure level is more than 240 dB from 0 to 100 kHz. The optimization effect of the ball-tipped needle-ring electrode is obvious. Using the ball-tipped needle-ring electrode structure as the discharge load of the impulse sound source can more effectively improve the performance of the impulse sound source so that it has the ability of long-distance and high-precision detection, which, in turn, improves the effect of its drilling acoustic wave logging application.

Figure 15. Sound pressure level–frequency plots for needle-ring electrode and ball-tipped needle-ring electrode.

Table 9. Comparison of ball-tipped needle-ring electrode and needle-ring electrode.

Electrode Structures	Pre-Breakdown Time	Breakdown Voltage	Maximum Discharge Current	Maximum Impulse Wave Amplitude	Electro-acoustic Conversion Efficiency
Needle-ring electrode	229.09 µs	18.96 kV	26.5 kA	20.73 MPa	2.56%
Ball-tipped needle-ring electrode	204.42 µs	19.48 kV	27.8 kA	21.20 MPa	2.79%

4.2. Prospects

The optimized ball-tipped needle-ring electrode is used as the discharge load of the impulse sound source, which can release strong amplitude impulse waves and still maintain high sound pressure in the frequency band of 0–100 kHz, and it can play an important role in the detection of the geological body in front of the drill bit during drilling. Table 10 summarizes and compares the transmitting and impulse sources of conventional acoustic logging in recent years.

Table 10. Summary of along-drill sonic depth detection technology.

Along-Drill Sonic Depth Detection Technology	Single Pole Transducer Longitudinal Wave Measurement	Dipole Transducer Transverse Wave Measurement	Phased-Array Transducer Azimuthal Measurement	Multipole Transducer Quadrupole Wave Measurement	Impulse Sound Source Shockwave Measurement
Bandwidth	10 kHz–20 kHz	0.5 kHz–5 kHz	around 14 kHz	1 kHz–25 kHz	controllable from 0 kHz to 300 kHz
Wave amplitude	high	medium	low	high	higher
Detection area	dozens of meters	tens of meters	tens of meters	tens of meters	hundred meters
Propagation loss	high	low	medium	low	frequency dependent, controllable
Sound source directivity	low	medium (axisymmetric)	high (directional emission)	medium (axisymmetric)	high (configurable)
Detection accuracy	high	low	medium	high	frequency dependent, controllable
Representative instruments	BARS [29], CLSS [30], Shockwave [31], CrossWave [32]	Sonic scanner [33], DSI [34], BAT [35], Wave sonic [36], MAC series [37]	Azimuthal remote detection sonic logging instrument (BAR) [38]	APX [39], QBAT and XBAT [40], SonicScope [41,42]	in the experimental and basic research stages, no commercialized instruments

Monopole transducers, dipole transducers, phased-array transducers, and multipole transducers have their own advantages and disadvantages in terms of the sound source frequency band, acoustic amplitude, spatial size limitation, sound source directivity, detection distance, and detection accuracy; however, it is not possible to combine them. The impulse sound source equipped with a ball-tipped needle-ring electrode can release strong energy. The frequency can be selected from 0 to 100 kHz according to the detection requirements. When describing small geological bodies in the near-well zone, high-frequency excitation can be selected, which provides higher accuracy. When detecting large geological bodies in the far-well zone, low-frequency excitation can be selected, which has a longer detection distance. Moreover, the ball-tipped needle-ring electrode is tiny, which is suitable for the narrow space and operation of the downhole instrument. Therefore, the impulse sound source has advantages and feasibility as the transmitting sound source of drilling acoustic logging.

However, the impulse source is currently in the experimental and basic research stage, and there is no commercial instrumentation yet. More theoretical basic research, physical experimental research, mathematical modeling analysis, and practical well-field applications are needed for the impulse sound source.

The main aspects are as follows:

(1) Electro-acoustic characteristics of the impulsive sound source: A study of the influence of external circuit parameters (such as charging voltage and storage capacity) and the downhole working environment (such as dielectric conductivity, high temperatures, and high hydrostatic pressure downhole) on the electro-acoustic characteristics of the sound source.

(2) Investigation of the directivity of the sound source: The impulse sound source can be equipped with a reflector to achieve directional energy concentration emission. Numerical simulation and evaluation experiments are required to assess the effect of the reflector on energy collection.

(3) Orthogonal evolution of borehole geology during drilling: The study of the influence law of geological body size, distance, angular position, reservoir type, and other parameters on the acoustic field and detection ability of the borehole to lay the foundation for the subsequent engineering problems of logging while drilling using the impulse sound source.

(4) Inversion of borehole geology while drilling: Acoustic data reception and processing. It is necessary to intercept the appropriate received data window according to the detection distance and the size of the emission frequency of the sound source.

(5) Harsh downhole working environment: The downhole must be tested at high temperatures (175 degrees Celsius) and high pressures (100 MPa) and is equipped with high-temperature- and high-pressure-resistant components. To ensure acoustic transmission efficiency and signal stability, it is necessary to improve the signal-to-noise ratio and configure the appropriate directional beam energy and frequency according to the detection requirements to achieve downhole detection without destroying the borehole.

5. Conclusions

Based on the traditional acoustic logging sound source, we introduced the impulse sound source as the emission sound source for drilling acoustic logging. A high-voltage experimental platform was constructed to evaluate the impulse sound source, and the sound source characteristics were obtained using a needle-bar electrode as the discharge load. Through numerical simulation, an electrode structure suitable for drilling acoustic logging was selected from four types of needle series electrodes, and the preferred electrode structure was further improved and optimized. The prospects and feasibility of the impulse sound source were analyzed, and recommendations were made for future work and applications. The main conclusions are as follows:

(1) Conventional mainstream transmitting sound sources, including monopole transducers, dipole transducers, phased-array transducers, and multipole transducers, have frequencies below 25 kHz and limited wave amplitudes, which cannot meet the future requirements of high-precision and long detection ranges in a well.

(2) The electrode structure, as the discharge load of the impulse sound source, can directly affect the performance of the impulse sound source. Through experiments and numerical simulations, it was obtained that among the needle series electrode structures, the intensity of the impulsive wave of the needle-ring electrode is higher, up to 20.73 MPa, and the electro-acoustic conversion efficiency is larger, which is more suitable for acoustic logging with drilling, as it possesses the characteristics of a wide bandwidth and high amplitude at the same time.

(3) The upgraded and optimized ball-tipped needle-ring electrode further improves the electro-acoustic performance. The intensity of the impulse wave was raised to 21.2 MPa and still maintained a high sound pressure in the frequency band of 0–100 kHz. The impulse acoustic source has the ability to detect geological areas of up to 100 meters away and is beneficial for the effective evaluation of micro-fractures and small fracture blocks adjacent to wells where high detection accuracy is required, which is of great importance in oil, gas, and new energy drilling.

(4) The impulse sound source has advantages and feasibility as a transmitting sound source for drilling acoustic logging. However, the impulse sound source is currently in its experimental and basic research stage, and there is no commercialized instrument. To develop the impulse sound source, it is necessary to conduct theoretical research, physical experiments, mathematical model analysis, and practical applications in well environments. For the development of the impulse sound source, theoretical basic

research, physical experimental research, mathematical model analyses, and practical well applications are needed.

Author Contributions: Conceptualization, J.Z.; methodology, X.G. and H.X.; formal analysis, X.G. and X.D.; investigation, X.G. and X.D.; resources, J.Z.; data curation, X.G. and H.X.; writing—original draft preparation, X.G.; writing—review and editing, J.Z. and H.X. All authors have read and agreed to the published version of the manuscript.

Data Availability Statement: The original contributions presented in the study are included in the article, further inquiries can be directed to the corresponding author.

Conflicts of Interest: The authors declare no conflicts of interest.

References

1. Zhan, W.; Chen, Y.; Liu, Q.; Li, J.; Sacchi, M.D.; Zhuang, M.; Liu, Q.H. Simultaneous prediction of petrophysical properties and formation layered thickness from acoustic logging data using a modular cascading residual neural network (MCARNN) with physical constraints. *J. Appl. Geophys.* **2024**, *224*, 105362. [CrossRef]
2. Yang, E.M.; Lv, G.W.; Wu, Y.; Cui, Z.-W.; Liu, J.-X. Numerical study of dispersion characteristics of dipole flexural waves in a cased hole with different cement conditions. *Appl. Geophys.* **2022**, *19*, 29–40.
3. Zhang, H.L.; Su, Y.D.; Wang, M.; Tang, X. Fluid conductivity in circumferential fractures and deliverability evaluation based on rock mechanics. *Geophys. Prospect. Pet.* **2024**, *63*, 207–216.
4. Shen, Q.Y.; Li, S.Q.; Cui, Y.J.; Su, Y.D.; Wang, P.C.; Tang, X.M. A New Comprehensive Well Logging Data Method for Evaluating Fracture Reservoir Productivity and Its Application. *Well Logging Technol.* **2023**, *47*, 152–160.
5. Stamatellou, A.-M. PZT and PVDF piezoelectric transducers' design implications on their efficiency and energy harvesting potential. *Energy Harvest. Syst.* **2023**, *10*, 157–167. [CrossRef]
6. Lee, J.S.; Kim, Y.H. Recent Advances in Piezoelectric Transducers for Borehole Applications. *IEEE Trans. Ultrason. Ferroelectr. Freq. Control* **2017**, *64*, 1251–1262.
7. Toledo, J.; Ruiz-Díez, V.; Diaz-Molina, A.; Ruiz, D.; Donoso, A.; Bellido, J.C.; Wistrela, E.; Kucera, M.; Schmid, U.; Hernando-García, J.; et al. Design and Characterization of In-Plane Piezoelectric Microactuators. *Actuators* **2017**, *6*, 19. [CrossRef]
8. Zhang, K.; Tan, B.; Zhang, W.; Sun, Y.; Zheng, J.; Su, Y.; Liu, X.; Wu, G.; Xin, S. Design of a New Acoustic Logging While Drilling Tool. *Sensors* **2021**, *21*, 4385. [CrossRef] [PubMed]
9. Chen, M.; Sun, D.Q.; Xie, X.H.; Gao, Y.L.; Wang, D.; Liu, J.H. Progress and prospect of acoustic logging while drilling technologies. *World Pet. Ind.* **2023**, *30*, 32–41.
10. Mickael, M.; Barnett, C.; Diab, M. Azimuthall-focused LWD Sonic Logging for Shear-wave Anisotropy Measurement and Borehole Imaging. In Proceedings of the SPE Annual Technical Conference and Exhibition, San Antonio, TX, USA, 8–10 October 2012.
11. Zhu, Z. The logging mode optimization and remote detection performance of monopole acoustic logging while drilling. *J. Appl. Acoust.* **2022**, *41*, 310–317.
12. Li, Y.H.; Tang, X.M.; Su, Y.D. Azimuthal response of the received wavefield in open and cased boreholes for dipole shear-wave reflection imaging. *Chin. J. Geophys.* **2022**, *65*, 4122–4140.
13. Tan, B.; Zhang, K.; Su, Y.; Li, S.; Zhang, L. Research on acoustic logging while drilling transmitting technologies. *J. Geophys. Eng.* **2022**, *3*, 511–520. [CrossRef]
14. Dubinsky, V.; Tang, X.M.; Bolshakov, A.; Patterson, D. Engineering aspects of LWD quadrupole measurements and field test results. In Proceedings of the SPE Annual Technical Conference and Exhibition, Denver, CO, USA, 5–8 October 2003.
15. Zhao, Q.; Che, X.; Qiao, W.; Tao, S.; Wang, J. Inversion of radial formation velocity distribution based on monopole acoustic logging while drilling. *Geoenergy Sci. Eng.* **2023**, *231*, 212–313. [CrossRef]
16. Cao, J.J.; Tang, X.M.; Su, Y.D. Radiation characteristics of a multipole acoustic source in an open borehole. *Tech. Acoust.* **2016**, *35*, 487–492.
17. Tan, B. *A Study of Multipole Acoustic Logging While Drilling Excitation and Acquisition Technology*; China University of Petroleum (East China): Jinan, China, 2019.
18. Wang, R.; Coates, R. Accurately Estimating Shear Slowness Using Data-Driven Quadrupole Sonic Logging-While- Drilling Data Processing. In Proceedings of the SPWLA 60th Annual Logging Symposium, The Woodlands, TX, USA, 15–19 June 2019.
19. Qiao, W.X.; Jv, X.D.; Che, X.H.; Lu, J.Q. Progress in Acoustic Well Logging Technology. *Well Logging Technol.* **2011**, *35*, 14–19.
20. Lu, J.Q.; Jv, X.D.; Men, B.Y.; Liu, X.P.; Yang, Z.X. Design of Electronic System of Far Detection Azimuthal Acoustic Logging Tool. *Well Logging Technol.* **2022**, *46*, 530–535.
21. Ben, J.L.; Che, X.H.; Qiao, W.X.; Jv, X.D.; Wang, Z.Y.; Lu, J.Q.; Men, B.Y. Application of Near-Borehole Geologic Reflector Evaluation Using Azimuthal Acoustic Reflection Imaging Logging. *Well Logging Technol.* **2021**, *45*, 23–29.
22. Zuo, C. *Research on the Measurement Resolution of Phased Array Acoustic Logging*; China University of Petroleum: Beijing, China, 2023.

23. Hao, X.; Zhou, J.; Shang, H.; Xie, H.; Wang, W.; Yang, C. A Plasma Transmitting Source for Borehole Acoustic Reflection Imaging. *Sensors* **2022**, *22*, 8050. [CrossRef] [PubMed]

24. Yu, G.; Jiang, N.; Peng, B.; Sun, H.; Liu, Z.; Li, J. Study on the plasma characteristics in a needle-plate dielectric barrier discharge with a rotating dielectric plate. *J. Appl. Phys.* **2023**, *133*. [CrossRef]

25. Wang, R.; Ji, Q.; Zhang, T.; Xia, Q.; Zhang, Y.; Ouyang, J. Discharge characteristics of a needle-to-plate electrode at a micro-scale gap. *Plasma Sci. Technol.* **2018**, *20*, 126–130. [CrossRef]

26. Zhou, G.Y. *Study on Influence of Shock Waves Induced by Underwater Pulse Current Discharges*; Huazhong University of Science and Technology: Hangzhou, China, 2018.

27. Yanshin, E.V.; Korobeynikov, S.M.; Ovchinnikov, I.T.; Sarin, S.G.; Yanshin, K.V.; Kopylov, V.M.; Klepikov, A.V. Physical processes limiting the pulse energy release in liquid dielectrics. In Proceedings of the 10th IEEE International Pulse Conference, Albuquerque, NM, USA, 3–6 July 1995; pp. 574–579.

28. Liu, Y.L.; Shang, S.H.; Jin, D.Z. Calculation of inductance of pulse discharge circuit. *J. Terahertz Sci. Electron. Inf. Technol.* **2018**, *16*, 724–728.

29. Aron, J.; Chang, S.K.; Codazzi, D.; Dworak, R.; Hsu, K.; Lau, T.; Minerbo, O.; Yogeswaren, E. Real-Time Somc Logging While Drilling In Hard And Soft Rocks. In Proceedings of the SPWLA 38th Annual Logging Symposium, Houston, TX, USA, 15–18 June 1997.

30. Schlumberger, G. *Geoframe BARS User' Guide*; Version 1.0; Schlumberger K K: Kanagawa, Japan, 1998; pp. 1–6.

31. Minear, J.; Birchak, R.; Robbins, C.; Linyaev, E.; Mackie, B.; Young, D.; Malloy, R. Compressional Slowness Measurements While Drilling. In Proceedings of the SPWLA 36th Annual Logging Symposium, Houston, TX, USA, 26–29 June 1995.

32. Kozak, M.; Boonen, P.; Seifert, D. Phase velocity processing for acoustic logging-while-drilling full waveform data. In Proceedings of the SPWLA 42nd Annual Logging Symposium, Houston, TX, USA, 17–20 June 2001.

33. Plona, T.J.; Kane, M.R.; Sinha, B.; Walsh, J. Evaluating stress-induced anisotropy and mechanical damage from cross-dipole sonic data using dispersion analysis. In Proceedings of the SPE/ISRM Rock Mechanics Conference, Irving, TX, USA, 20–23 October 2002.

34. Pistre, V.; Kinoshita, T.; Endo, T.; Schilling, K.; Pabon, J. A Modular Wireline Sonic Tool for Measurements of 3D (Azimuthal, Radial, and, Axial) Formation Acoustic Properties. In Proceedings of the SPWLA 46th Annual Logging Symposium, New Orleans, LA, USA, 26–29 June 2005.

35. Arian, A.; Althoff, G.; Varsamis, G.L.; Wisniewski, L.T. A new MWD full wave dual mode sonic tool design and case histories. In Proceedings of the SPWLA 40th Annual Logging Symposium, Oslo, Norway, 30 May–3 June 1999.

36. Bonavides, C. *WaveSonic CookBook*, 5th ed.; Halliburton: Houston, TX, USA, 2001.

37. Joyce, B.; Patterson, D.; Leggett, J.; Dubinsky, V. Introduction of a new omni-directional acoustic system for improved real-time LWD sonic logging-tool design and field test results. In Proceedings of the SPWLA 42nd Annual Logging Symposium, Houston, TX, USA, 17–20 June 2001.

38. Xie, C.; Men, B.Y.; Yao, Y.C.; Lu, J.Q.; Wang, B.W.; Liu, X.P. Design of Data Reading Interface for the Borehole Azimuth Acoustic Reflectiion Imaging Tool Based on USB Bus. *Comput. Meas. Control* **2021**, *29*, 218–222.

39. Tang, X.M.; Dubinsky, V.; Wang, T.; Bolshakov, A.; Patterson, D. Shear-velocity measurement in the Logging-While-Drilling environment: Modeling and field evaluations. *Petrophysics* **2003**, *2*, 79–90.

40. Market, J. New broad frequency LWD multipole tool provides high quality compressional and shear data in a wide variety of formations. In Proceedings of the SPWLA 48th Annual Logging Symposium, Austin, TX, USA, 3–6 June 2007.

41. Kinoshita, T.; Endo, T.; Nakajima, H.; Yamamoto, H.; Dumont, A.; Hawthorn, A.; Oilfield, S. Next generation LWD sonic tool. In Proceedings of the 14th Formation Evaluation Symposium of Japan, Chiba, Japan, 29–30 September 2008.

42. Oil, Gas & Petrochem Equipment Group. Multioole sonic-while-drilling. *Oil Gas Petrochem Equip.* **2013**, *60*, 12.